Lawrence Berkeley National Laboratory
LBL Publications

Title
Inverse Biot–Savart Optimization for Superconducting Accelerator Magnets

Permalink
https://escholarship.org/uc/item/02x5z351

Journal
IEEE Transactions on Magnetics, 57(9)

ISSN
0018-9464

Authors
Teyber, Reed
Brouwer, Lucas
Qiang, Ji
et al.

Publication Date
2021-09-01

DOI
10.1109/tmag.2021.3092527

Peer reviewed

Inverse Biot–Savart Optimization for Superconducting Accelerator Magnets

Reed Teyber[ID], Lucas Brouwer[ID], Ji Qiang, and Soren Prestemon[ID]

Lawrence Berkeley National Laboratory (LBNL), Berkeley, CA 94720 USA

   Superconducting (SC) magnets for accelerator concepts are often synthesized by numerically optimizing magnetic field waveforms, a process that requires a subsequent solution of a constrained inverse problem to identify suitable SC magnet windings. When the desired field distribution is intuitive, the inverse process is facilitated by seeding preconceived coil distributions into design optimization methods for refinement. With more complex magnetic field distributions, an initial design may be unknown, and topology optimization tools are required to synthesize current distributions without *a priori* guidance from a subject matter expert. In this work, we develop a constrained inverse Biot–Savart topology optimization methodology that synthesizes optimal distributions of current density in racetrack-like SC coils. The problem structure is exploited through a computationally efficient quadratic programming formulation, and the method is applied to recently published magnetic field waveforms for a recirculating proton phase shifter, a proton therapy gantry, and dipole magnets with sharp field transitions. The method and results herein identify novel winding configurations that can help magnet designers bring accelerator concepts to fruition.

I. INTRODUCTION

Accelerator magnet concepts are typically synthe-sized by numerically optimizing beam dynamics codes as a function of magnetic fields, however the resulting distribution of current and magnetic material that produces this field waveform must be identified through an inverse process. If the prescribed magnetic field is intuitive (e.g. harmonic), a subject matter expert can suggest preconceived magnet designs and use design optimization methods for iterative refinement. When a magnetic field distribution is more complex, a subject matter expert's attempt at an initial magnet design may be far from optimal or altogether infeasible. In these cases, there is a need for topology optimization tools to synthesize current distributions for the desired magnetic field distribution without *a priori* knowledge of candidate designs. The synthesized current distributions can then be used to motivate realizable winding concepts or to seed conventional magnet optimization processes.

Insinga has reported extensively on the inverse design of magnet systems with an emphasis on the reciprocity theorem [1], [2], and a number of optimization methodologies have been reported across a range of magnet disciplines [3]–[6]. Instead of solving finite-element codes for the diffusion of magnetic potentials, coil-dominated superconducting (SC) magnets can be evaluated with computationally efficient Biot–Savart techniques for current-field inversion [7]–[14].

In this work, we develop an inverse Biot–Savart topology optimization method to identify current distributions for prescribed magnetic fields when feasible magnet concepts are unknown. The problem structure is exploited through a computationally efficient bounded quadratic programming formulation that imposes balanced current return paths in the design domain. The developed tool is used to synthesize current distributions for previously reported large momentum acceptance magnets and pure dipole fields.

The manuscript is organized as follows. The magnetic layout and design domain are introduced before describing the midplane field distribution as a matrix system based on the Biot–Savart law. The problem is then formulated as a convex optimization to improve numerical stability. Next, synthesized current distributions for a recirculating proton phase shifter are presented. Optimization results are then presented for a proton therapy gantry with an emphasis on reducing numerical instabilities and oscillatory behavior. The final case study explores a dipole magnet with sharp field transitions, motivating a discussion of the methodology.

II. METHODS

A. Magnet Layout

Brouwer *et al.* [15] developed a new SC magnet and beam dynamics solution capable of transporting 70–225 MeV protons with fixed-field for proton therapy gantries (Fig. 1). More recently, the concept was extended to a phase shifter for multi-pass recirculating proton linear accelerators with energies between 150 MeV and 2 GeV (Fig. 2) [16]. In both applications, the beam enters the side of two vertical-field magnets forming a symmetric system where particles are delivered to a fixed location regardless of beam energy. The beam energies illustrated in yellow, pink, and purple show higher-energy protons penetrating deeper into the magnet.

In Figs. 1 and 2, cross sections A-A reveal SC windings that resemble long racetrack coils. This cross section is illustrated in Fig. 3 and defines the design domain for the inverse
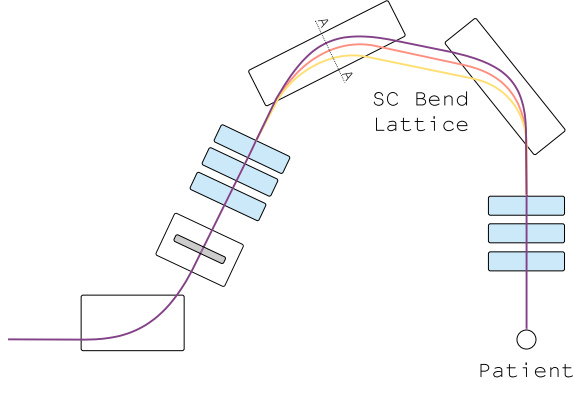
Fig. 1. Fixed-field proton therapy gantry with large momentum acceptance SC magnets. Higher beam energies (purple) penetrate further into magnet. Section A-A reveals a magnet cross section resembling Fig. 3.
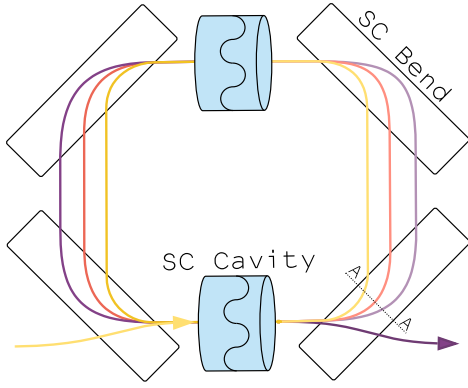

Fig. 2. Recirculating proton phase shifter with large momentum acceptance SC magnets. Higher beam energies (purple) penetrate further into magnet. Section A-A reveals a magnet cross section resembling Fig. 3.

Biot–Savart topology optimization. Fig. 3 shows discretized top and bottom coil domains that produce a vertical magnetic field along a discretized midplane. Each discretized domain takes a continuous value of current, ranging between negative (blue, $-J$), air (white, $J = 0$), and positive (red, $+J$). The domain width and height are prescribed, and the current density is lumped at the center of each discrete domain using a uniform grid (fixed Δx, Δy). The desired vertical magnetic field at each of k midplane points is supplied by a beam dynamics optimization and is invariant along the magnet length (z). The resulting distribution of current at each block i, j must be solved in a manner in which the net amount of current is balanced.

B. Inverse Biot-Savart

As shown in Fig. 3, every current element in the top and bottom discretized coil domain (i, j) contributes to the magnetic field at each of k components along the discretized midplane axis. Assuming infinitely long wires, the resulting vertical magnetic field at a single discrete point k is found by summing the magnetic field over all (i, j) discrete
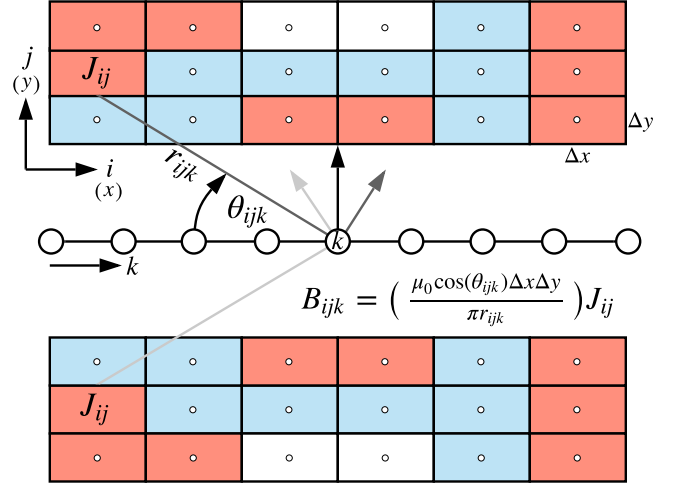

Fig. 3. 2-D domain for inverse Biot–Savart optimization. Symmetric windings produce a vertical magnetic field along discretized midplane axis. Current densities are lumped into line currents (center circle in each element) for evaluation of Biot–Savart law. Each discretized domain takes a continuous value of current, ranging between negative ($-J$), air (white, $J = 0$), and positive (red, $+J$).

current elements

$$B_k = \sum_{i}^{n_i} \sum_{j}^{n_j} \left(\frac{\mu_0 \cos(\theta_{ijk}) \Delta x \Delta y}{\pi r_{ijk}} \right) J_{ij} \tag{1}$$

where θ_{ijk} and r_{ijk} are the angle and radius between current element (i, j) and point k along the discretized midplane axis. The inverse problem is solved when the error between this current-produced magnetic field and the prescribed magnetic field is minimized over all k points.

At each discretized point, the magnetic field is a linear function of the current density J_{ij}:

$$B_k = \sum_{i,j} B_{ijk}^* J_{ij} \tag{2}$$

where B_{ijk}^* is (1) evaluated with unit current density (or the maximum allowable current density, e.g., 500 A/mm²) for current element ij at midplane field node k and J_{ij} is the corresponding current density. This can be rewritten as the vector multiplication of a flattened B_{ijk}^* matrix (different matrix at each k) and flattened current density array J_{ij}, and this summation must equal the prescribed vertical magnetic field at midplane point B_k^p. For many prescribed midplane points, this can be expressed in matrix form as

$$\begin{bmatrix} B_{000}^* & B_{ij0}^* & B_{n_i n_j 0}^* \\ B_{00k}^* & B_{ijk}^* & B_{n_i n_j k}^* \\ B_{00n_k}^* & B_{ijn_k}^* & B_{n_i n_j n_k}^* \end{bmatrix} \begin{bmatrix} J_{00} \\ J_{ij} \\ J_{n_i n_j} \end{bmatrix} = \begin{bmatrix} B_0^p \\ B_k^p \\ B_{n_k}^p \end{bmatrix} \tag{3}$$

which is of the form $AJ = b$. Each row in matrix A corresponds to a prescribed magnetic field point k, and each column corresponds to a current element to be resolved at location ij. To create a magnet design tool based on wound SC coils, the realistic constraint of balanced current must be

adhered to

$$\sum_{i,j} J_{ij} = 0 \tag{4}$$

which can be written as the vector multiplication of a unit array and the flattened J_{ij} matrix (i.e., $c^{\mathrm{T}}J = 0$). As the balanced current constraint is linear, it can be augmented into the $AJ = b$ matrix system

$$\begin{bmatrix} B_{000}^* & B_{ij0}^* & B_{n_in_j0}^* \\ B_{00k}^* & B_{ijk}^* & B_{n_in_jk}^* \\ B_{00n_k}^* & B_{ijn_k}^* & B_{n_in_jn_k}^* \\ 1 & 1 & 1 \end{bmatrix} \begin{bmatrix} J_{00} \\ J_{ij} \\ J_{n_in_j} \end{bmatrix} = \begin{bmatrix} B_0^p \\ B_k^p \\ B_{n_k}^p \\ 0 \end{bmatrix}. \tag{5}$$

For familiarity, we will interchangeably refer to the augmented B_{ijk}^* matrix as A and the augmented prescribed magnetic field array B_k^p as b. Given an excess of discretized current elements ($n_in_j > n_k$), one can solve the overdetermined least-squares problem to obtain the current distribution generating the prescribed magnetic field along the magnet midplane. It was found that the current density needed bounds to produce physically realistic coils, which gave rise to a bounded least-squares optimization

$$\text{Min } ||AJ - b||_2^2 \quad -1 \leq J \leq 1. \tag{6}$$

One can rewrite the least-squares objective as

$$||AJ - b||_2^2 = J^{\mathrm{T}}A^{\mathrm{T}}AJ - J^{\mathrm{T}}A^{\mathrm{T}}b - b^{\mathrm{T}}AJ + b^{\mathrm{T}}b \tag{7}$$

which can be expressed as a convex quadratic programming (QP) problem

$$\text{Min } \frac{1}{2}J^{\mathrm{T}}PJ + q^{\mathrm{T}}J \quad -1 \leq J \leq 1 \tag{8}$$

with $P = A^{\mathrm{T}}A$ and $q = -A^{\mathrm{T}}b$. The optimization problem is solved using the operator splitting quadratic program (OSQP) [17] in the framework of CVXPY [18]. This formulation has reduced numerical instabilities stemming from the ill-conditioned system.

III. Results

A. Proton Phase Shifter

The first example investigates the magnetic field distribution reported in [16] for a four-pass proton phase shifter [19], [20]. The magnetic field profile is defined by (9) and is the result of an optimization to satisfy the synchronous condition for SC radio frequency (RF) cavities

$$B_y(x) = \begin{cases} 0, & x < 0 \\ 2.5\left(\tanh\left(20\pi(x-0.05)\right)+1\right), & 0 \leq x \leq 0.1 \\ 5 - 37.45(x - 0.1)^2 \cdots \\ \quad +78.45(x-0.1)^3 \cdots \\ \quad +68.02(x-0.1)^4 \cdots \\ \quad +6.69(x-0.1)^5, & x > 0.1. \end{cases} \tag{9}$$

For all results in this article, the prescribed magnetic field waveform is discretized into $n_k = 300$ points, and the coil domain is discretized into $n_i = 200$ and $n_j = 100$ points. This yields a constrained optimization of 20 000 variables and a
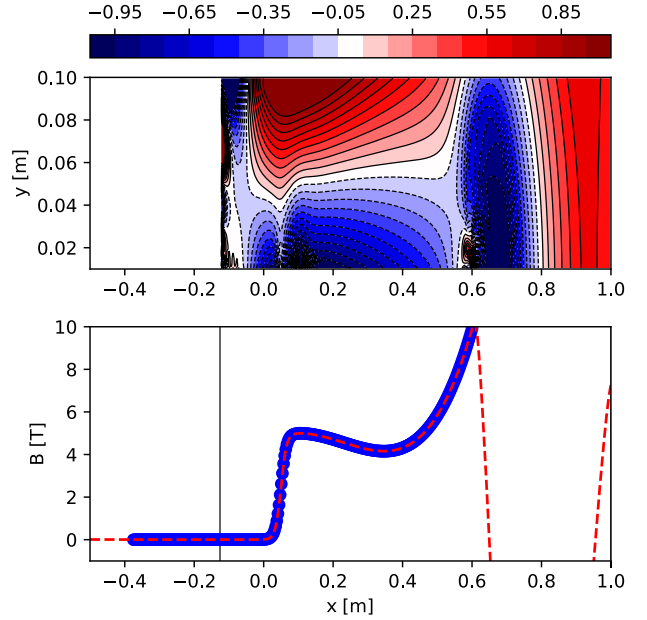

Fig. 4. Optimized current distribution for a large momentum acceptance proton phase shifter with reduced current domain height (100 mm). Top plot shows the synthesized current distribution (see Fig. 3), and the color bar values of ± 1 correspond to $J = \pm 500$ A/mm². Bottom plot shows the prescribed, discrete magnetic field distribution in blue circles (9) and the red dashed line shows the Biot–Savart calculated magnetic field.

dense A matrix of 6 million elements, which is typically solved in 1–2 min on a desktop computer. The Biot–Savart matrix is scaled so that values of $J = \pm 1$ yield current densities of ± 500 A/mm², a common value in SC magnets. In all of the results presented here, the coil design domain is 10 mm from the midplane to allow for a small vacuum chamber.

The resulting optimization is shown in Figs. 4–6 for coil domain heights of 100, 200, and 300 mm, respectively. The x-axis coil domain limits are determined through an iterative process to balance application-specific constraints with field quality. In each figure, the top plot shows contours of the synthesized current density where a symmetric coil is implied (see Fig. 3). The bottom plot shows the prescribed, discrete magnetic field distribution in blue circles (9) and the red dashed line shows the Biot–Savart calculated magnetic field from the optimized current density in the top plot.

The optimized current distributions do an excellent job of producing the prescribed magnetic field, evidenced by the overlapping curves in the figures. High-frequency current density oscillations are observed in the bottom of each coil domain; methods to improve stability are discussed in the following section. The shortest domain height (Fig. 4) yields current densities tending toward the bounds $J = \pm 1$. This facilitates realization as a windable magnet concept; one could envisage the contours of Fig. 4 replaced with a horizontally wound coil along the right of the domain, a vertically wound coil in the center of the domain and a series of vertically wound coils along the left of the domain. Finally, it is observed that the majority of red contours lie on the right side of the domain where the contribution to the field waveform is minimized; this is to satisfy the balanced current constraint.
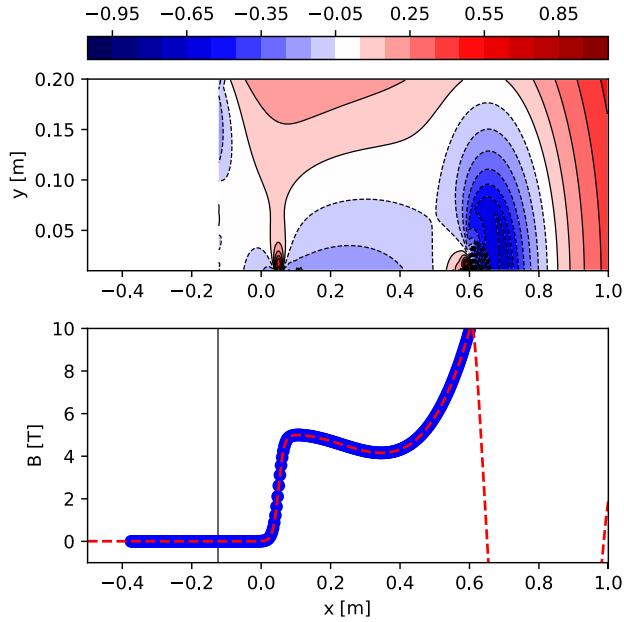
Fig. 5. Optimized current distribution for a large momentum acceptance proton phase shifter with 200 mm domain height. Top plot shows the synthesized current distribution (see Fig. 3), and the color bar values of ± 1 correspond to $J = \pm 500$ A/mm^2. Bottom plot shows the prescribed, discrete magnetic field distribution in blue circles (9) and the red dashed line shows the Biot–Savart calculated magnetic field.
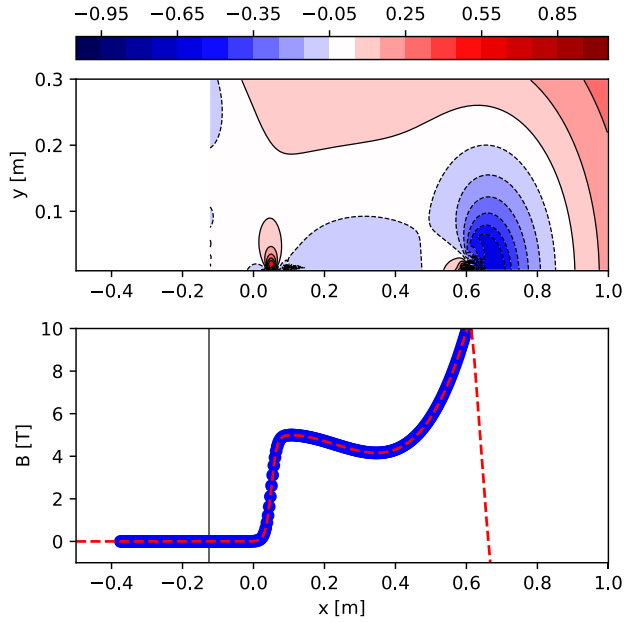

Fig. 6. Optimized current distribution for a large momentum acceptance proton phase shifter with increased current domain height (300 mm). Top plot shows the synthesized current distribution (see Fig. 3), and the color bar values of ± 1 correspond to $J = \pm 500$ A/mm^2. Bottom plot shows the prescribed, discrete magnetic field distribution in blue circles (9) and the red dashed line shows the Biot–Savart calculated magnetic field.

Fig. 7 shows the impact of the coil discretization (number of optimization variables with $n_j = 2n_i$) on the condition number (black solid line, left y-axis) and magnetic field error (blue dashed line, right y-axis). The condition number is evaluated as $||A||_2 \cdot ||A^{-1}||_2$ using singular value decomposition
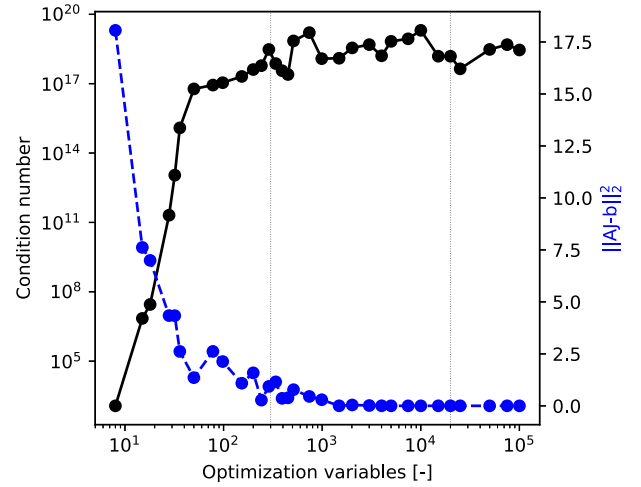

Fig. 7. Impact of mesh size on condition number of A matrix (left y-axis, solid black line on log scale) and error in optimized field (right y-axis, blue dotted line on linear scale). All points evaluated with the current domain of Fig. 5 (9) and with $n_j = 2n_i$.

FITTING PARAMETERS OF (10) FOR GANTRY MAGNET FROM BROUWER *et al.* [15]. FIT IS VALID IN RANGE $-0.1 \leq x \leq 0.3$. FIELD UNITS ARE TESLA AND x UNITS ARE IN METERS

Variable	Value
a_1	3.3404996
b_1	0.06929869
c_1	0.06215859
a_2	-0.38661478
b_2	-0.01048716
c_2	0.03229055
a_3	2.5330187
b_3	0.1783478
c_3	0.06390801

[with (5)], which is a proxy for the sensitivity of the solved current distribution (J) to small changes in the prescribed midplane magnetic field (b). The ill-conditioned matrix system is common in integral problems. The left vertical dotted line indicates where the number of current variables ($n_i n_j$) equals the number of prescribed field locations (n_k), and the right vertical dotted line indicates the number of optimization variables used throughout the manuscript. Field errors decrease rapidly with the number of optimization variables, where improvements are marginal beyond 1000 current elements.

B. Proton Therapy Gantry

The next case study is the magnetic field profile of Brouwer *et al.* [15] for a large momentum acceptance proton therapy gantry. Although the original magnet design consists of an iron-core Nb–Ti magnet, we apply the inverse Biot–Savart topology optimization to demonstrate the recreation of optics optimized magnetic field distributions. The magnetic field profile is approximated by the three Gaussian functions in (10) and Table I

$$B_y(x) = a_1 e^{-\left(\frac{x-b_1}{c_1}\right)^2} + a_2 e^{-\left(\frac{x-b_2}{c_2}\right)^2} + a_3 e^{-\left(\frac{x-b_3}{c_3}\right)^2}. \quad (10)$$
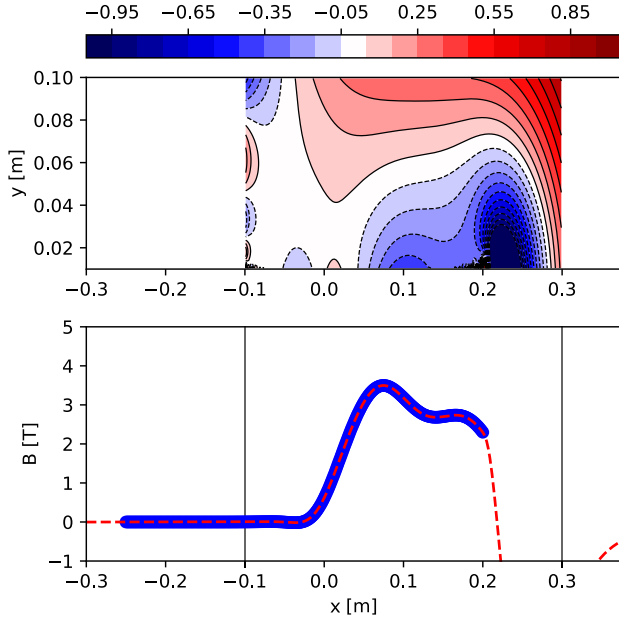
Fig. 8. Optimized current distribution for large momentum acceptance proton therapy gantry. Top plot shows the synthesized current distribution (see Fig. 3), and the color bar values of ± 1 correspond to $J = \pm 500$ A/mm². Bottom plot shows the prescribed, discrete magnetic field distribution in blue circles (10) and the red dashed line shows the Biot–Savart calculated magnetic field. Benchmark case (no filtering, no regularization) yields field quality of $||AJ - b||_2^2 = 0.003$.

Fig. 9. Optimized current distribution for large momentum acceptance proton therapy gantry. Top plot shows the synthesized current distribution (see Fig. 3), and the color bar values of ± 1 correspond to $J = \pm 500$ A/mm². Bottom plot shows the prescribed, discrete magnetic field distribution in blue circles (10) and the red dashed line shows the Biot–Savart calculated magnetic field. Gaussian-filtered case ($\sigma = 2$) yields field quality of $||AJ - b||_2^2 = 0.120$.

The optimized field profile in Fig. 8 shows strong agreement between prescribed and synthesized field waveforms, however high-frequency current oscillations are again observed along the bottom coil domain boundary. Two methods are briefly explored for reducing these variations in current density. The first approach is to filter the optimized current density using a 2-D Gaussian filter (SciPy). Fig. 9 shows the result with a Gaussian kernel standard deviation of $\sigma = 2$ pixels, where high-frequency oscillations at the bottom of Fig. 8 are effectively removed. The simplified design does come at the expense of decreased field quality, where $||AJ - b||_2^2$ increases from 0.003 to 0.120.

The second method to improve numerical stability is Tikhonov regularization (11), where the objective function is augmented with a penalization of the current density norm; this optimization can be solved with the same OSQP solver

$$\text{Min } ||AJ - b||_2^2 + \gamma ||J||_2^2 \quad -1 \leq J \leq 1. \tag{11}$$

Fig. 10 shows the regularized optimization with $\gamma = 0.01$, yielding a field error of $||AJ - b||_2^2 = 0.084$. While the Gaussian filter simply blends existing features, the Tikhonov regularization yields a new current distribution with differences most visible along the left boundary. Both filtering and regularization are effective in reducing the complexity of synthesized coils; however, the impact of field errors on beam behavior must be quantified using beam dynamics codes.

C. Dipole Magnet

A pure dipole field is now investigated with a focus on producing sharp magnetic features and exploring the impact
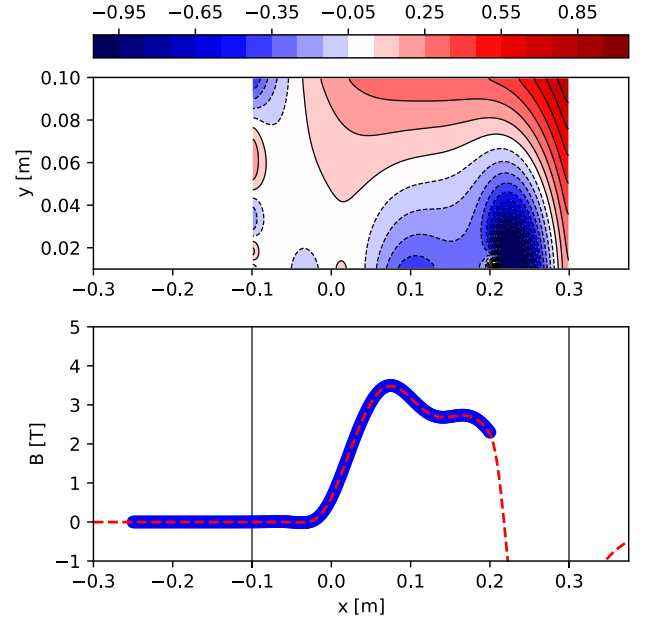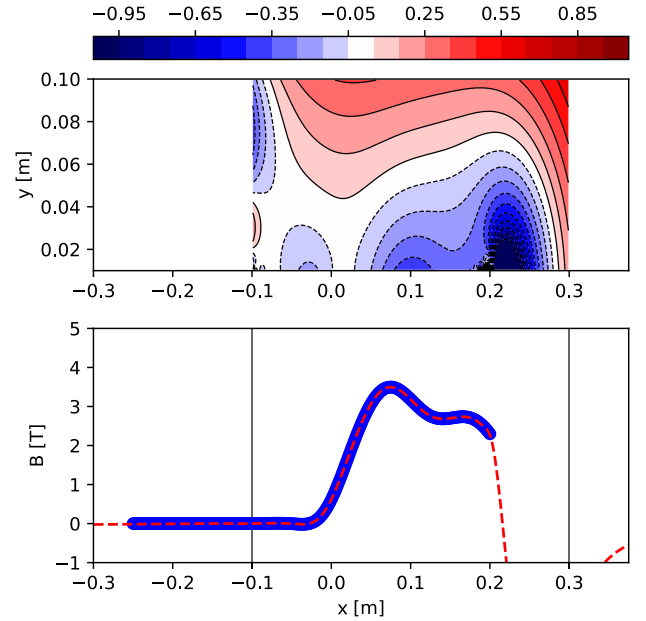

Fig. 10. Optimized current distribution for large momentum acceptance proton therapy gantry. Top plot shows the synthesized current distribution (see Fig. 3), and the color bar values of ± 1 correspond to $J = \pm 500$ A/mm². Bottom plot shows the prescribed, discrete magnetic field distribution in blue circles (10) and the red dashed line shows the Biot–Savart calculated magnetic field. Tikhonov regularization case [(11) with $\gamma = 0.01$] yields field quality of $||AJ - b||_2^2 = 0.084$.

of prescribed field domains. The target magnetic field is a pure 3 T dipole that immediately falls to 0 T beyond $x = \pm 0.25$ m, and no filtering or regularization is employed. The optimization result is shown in Fig. 11 for a prescribed field
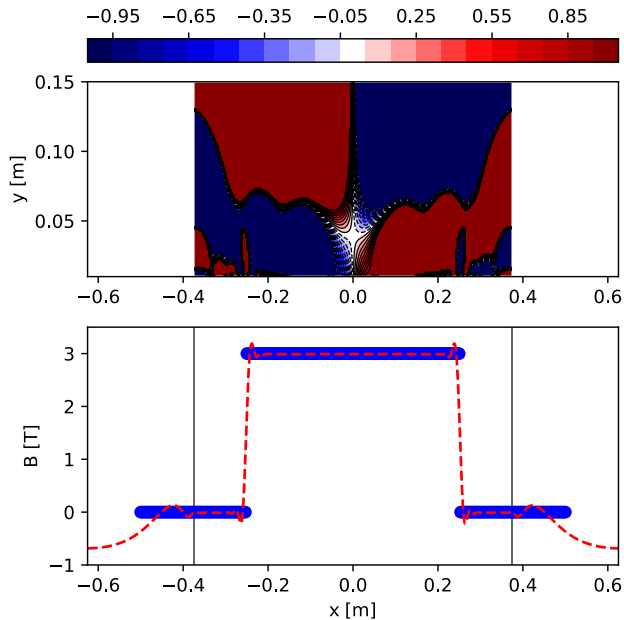
Fig. 11. Optimized current distribution for dipole field with step change to extended 0 T region. Top plot shows the synthesized current distribution (see Fig. 3), and the color bar values of ± 1 correspond to $J = \pm 500$ A/mm^2. Bottom plot shows the prescribed, discrete magnetic field distribution in blue circles and the red dashed line shows the Biot–Savart calculated magnetic field. Prescribed field (blue circles) extends beyond coil design domain (vertical gray lines).
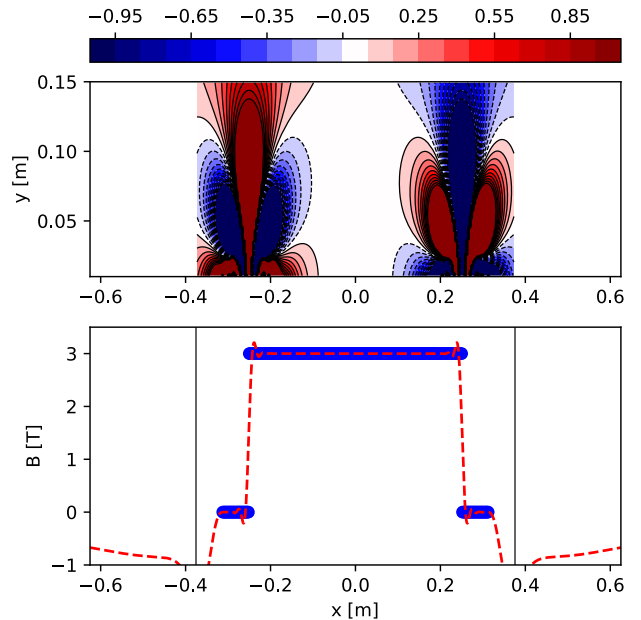

Fig. 12. Optimized current distribution for dipole field with step change to brief 0 T region. Top plot shows the synthesized current distribution (see Fig. 3), and the color bar values of ± 1 correspond to $J = \pm 500$ A/mm^2. Bottom plot shows the prescribed, discrete magnetic field distribution in blue circles and the red dashed line shows the Biot–Savart calculated magnetic field. Prescribed field (blue circles) lies within coil design domain (vertical gray lines).

region extending to $x = \pm 0.5$ m. The first observation is the nearly discrete nature of current density; each optimization variable tends toward the minimum or maximum bound of $J = \pm 1$. On the one hand, this is favorable in that discrete current densities lend to realistic and windable coil designs, and the result here can be realized as two counter-wound, vertically stacked SC coils. On the other hand, the discrete (i.e., bounded) optimization variables are a consequence of the optimizers inability to produce sharp features in the target design.

Fig. 12 shows the same optimization with a reduced zero field length of $x = \pm 0.3125$ m which now falls inside the coil domain of $x = \pm 0.375$ m. Air regions are observed in the coil domain, and current density clusters appear that resemble ensembles of oppositely wound coil blocks.

Fig. 13 shows an optimization with the zero-field region eliminated, leaving a pure dipole field. The optimized current density resembles a single racetrack coil with a shape-optimized boundary that increases field homogeneity. Note that by eliminating the sharp transition to 0 T, the required amount of current ($||J||_2^2$) decreases substantially; both Figs. 11 and 13 produce a high-field region of 3 T, however the cost of producing the two magnets varies greatly.

Fig. 14 shows the effect of the prescribed field width on the condition number (black solid line, left y-axis) and magnetic field error (blue dashed line, right y-axis). As in Fig. 7, the condition number is calculated with the augmented A matrix (balanced current constraint included in the last row). At $x = 0.25$ (left gray vertical line), the sharp transition to 0 T is imposed and a large increase in field error is observed. The
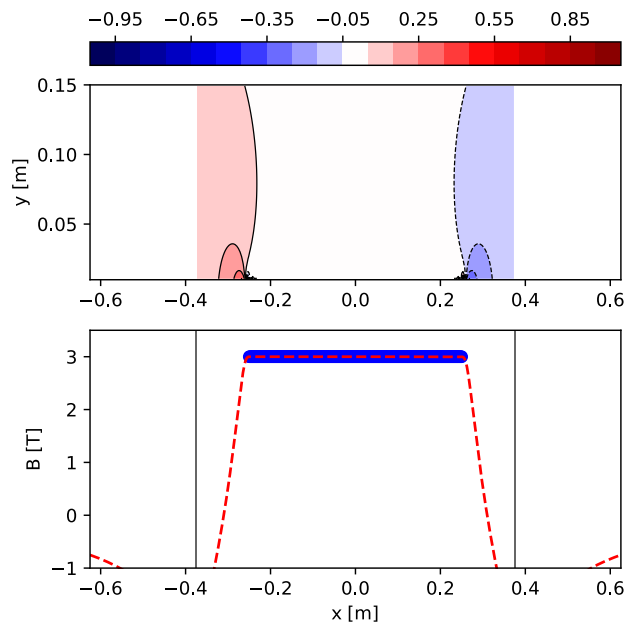

Fig. 13. Optimized current distribution for pure dipole field with no transition. Top plot shows the synthesized current distribution (see Fig. 3), and the color bar values of ± 1 correspond to $J = \pm 500$ A/mm^2. Bottom plot shows the prescribed, discrete magnetic field distribution in blue circles and the red dashed line shows the Biot–Savart calculated magnetic field. Prescribed field (blue circles) lies within coil design domain (vertical gray lines).

condition number increases rapidly when the prescribed field extends beyond the coil domain (middle vertical gray line).

IV. DISCUSSION

Comparing the three dipole coils of Figs. 11–13, the optimization is most effective when the current domain completely
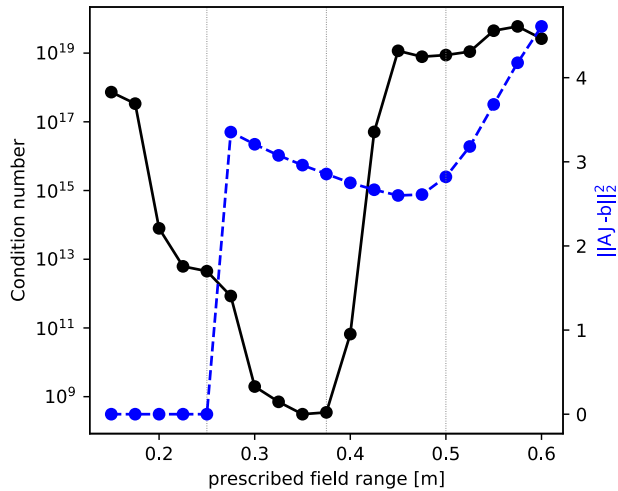
Fig. 14. Condition number (left y-axis, solid black line on the log scale) and error in desired field waveform (right y-axis, blue dotted line on linear scale) as a function of the prescribed field range for the dipole magnet. x-axis corresponds to the width of the prescribed field range for the dipole field with immediate transition to 0 T; $x = 0.25$ corresponds to Fig. 13, $x = 0.375$ corresponds to Fig. 12, and $x = 0.5$ corresponds to Fig. 11.

encompasses the desired field region (i.e., blue circles lie within left–right region of the coil domain). This is not an issue for typical coil design applications; however, this poses a challenge for large momentum acceptance SC magnets. As shown in the illustrative schematics of Figs. 1 and 2, accelerated protons enter the side of each magnet in the optics system. This means that the magnetic field must remain at 0 T to the left of the desired zero-field region (in the context of Figs. 5–8). In this layout, the coil domain cannot completely enclose the desired high-field region, and care must be taken to force a zero field region adequately far into the charged particle approach (i.e., left of domain).

Although the main limitation of the approach presented here is the continuous treatment of current density, the methodology provides value by motivating winding concepts and generating seed designs for conventional magnet optimization methods. Future research efforts will explore methods that synthesize discrete and windable coils with balanced current that produce desired magnetic field distributions.

V. Conclusion

The developed inverse Biot–Savart topology optimization method is a computationally efficient, flexible inverse design tool that has the potential to find new SC winding solutions that are previously unknown. Novel current distributions are rapidly synthesized for a recirculating proton linac, a proton therapy gantry and dipole fields with sharp edge transitions without *a priori* knowledge of candidate designs, giving direct feedback to magnet designers and beam physicists. Diverse field profiles are accurately reproduced, and the importance of coil domains that encompass the prescribed field region are discussed. Future work will explore discrete solutions to the problem investigated herein.

References

[1] A. R. Insinga, R. Bjørk, A. Smith, and C. R. H. Bahl, "Globally optimal segmentation of permanent-magnet systems," *Phys. Rev. A, Gen. Phys.*, vol. 5, no. 6, Jun. 2016, Art. no. 064014.

[2] A. R. Insinga, A. Smith, C. R. H. Bahl, K. K. Nielsen, and R. Bjørk, "Optimal segmentation of three-dimensional permanent-magnet assemblies," *Phys. Rev. A, Gen. Phys.*, vol. 12, no. 6, Dec. 2019, Art. no. 064034.

[3] J. Lee, S.-W. Lee, K. Kim, and J. Lee, "Multi-material topology optimization of magnetic actuator with segmented permanent magnets," *IEEE Trans. Magn.*, vol. 54, no. 7, pp. 1–6, Jul. 2018.

[4] R. Bjørk, C. R. H. Bahl, and A. R. Insinga, "Topology optimized permanent magnet systems," *J. Magn. Magn. Mater.*, vol. 437, pp. 78–85, Sep. 2017.

[5] R. Teyber, P. V. Trevizoli, T. V. Christiaanse, P. Govindappa, I. Niknia, and A. Rowe, "Permanent magnet design for magnetic heat pumps using total cost minimization," *J. Magn. Magn. Mater.*, vol. 442, pp. 87–96, Nov. 2017.

[6] H. Sasaki and H. Igarashi, "Topology optimization accelerated by deep learning," *IEEE Trans. Magn.*, vol. 55, no. 6, pp. 1–5, Jun. 2019.

[7] S. Russenschuck, T. Tortschanoff, A. Ijspeert, R. Perin, and N. Siegel, "Tracing back measured magnetic field imperfections in LHC magnets by means of the inverse problem approach," *IEEE Trans. Magn.*, vol. 30, no. 4, pp. 1797–1800, Jul. 1994.

[8] S. Caspi, M. Helm, and L. J. Laslett, "The 'inverse problem' to the evaluation of magnetic fields," *IEEE Trans. Magn.*, vol. 32, no. 4, pp. 2978–2981, Jul. 1996.

[9] J. van Nugteren *et al.*, "Idealized coil cross sections with minimized conductor area for high field dipoles," *IEEE Trans. Appl. Supercond.*, vol. 28, no. 3, pp. 1–5, Apr. 2018.

[10] F. Bellina, P. Campostrini, G. Chitarin, A. Stella, and F. Trevisan, "Automated optimal design techniques for inverse electromagnetic problems," *IEEE Trans. Magn.*, vol. 28, no. 2, pp. 1549–1552, Mar. 1992.

[11] A. Nijhuis, Y. A. Ilyin, and H. H. J. T. Kate, "Analysis of the current distribution in the ITER CS-insert model coil conductor by self field measurements," *IEEE Trans. Appiled Supercond.*, vol. 12, no. 1, pp. 1675–1679, Mar. 2002.

[12] Y. Ilyin and A. Nijhuis, "Review of current distribution measurements and reconstruction in cable-in-conduit conductors for ITER," *IEEE Trans. Appl. Supercond.*, vol. 17, no. 2, pp. 1465–1468, Jun. 2007.

[13] K.-H. Hauer, R. Potthast, and M. Wannert, "Algorithms for magnetic tomography—On the role of *a priori* knowledge and constraints," *Inverse Problems*, vol. 24, no. 4, Aug. 2008, Art. no. 045008.

[14] M. S. Poole and N. J. Shah, "Convex optimisation of gradient and shim coil winding patterns," *J. Magn. Reson.*, vol. 244, pp. 36–45, Jul. 2014.

[15] L. Brouwer, A. Huggins, and W. Wan, "An achromatic gantry for proton therapy with fixed-field superconducting magnets," *Int. J. Mod. Phys. A*, vol. 34, no. 36, Dec. 2019, Art. no. 1942023.

[16] J. Qiang, L. Brouwer, and S. Prestemon, "A phase shifter for multi-pass recirculating proton LINAC," in *Proc. 10th Int. Part. Accel. Conf.*, 2019, pp. 1–4.

[17] B. Stellato, G. Banjac, P. Goulart, A. Bemporad, and S. Boyd, "OSQP: An operator splitting solver for quadratic programs," *Math. Program. Comput.*, vol. 12, no. 4, pp. 637–672, Feb. 2020.

[18] S. Diamond and S. Boyd, "CVXPY: A Python-embedded modeling language for convex optimization," *J. Mach. Learn. Res.*, vol. 17, no. 83, pp. 1–5, 2016.

[19] J. Qiang, "Wide energy bandwidth superconducting accelerating cavities," *Nucl. Instrum. Methods Phys. Res. A, Accel. Spectrom. Detect. Assoc. Equip.*, vol. 795, pp. 77–81, Sep. 2015.

[20] J. Qiang, L. Brouwer, and R. Teyber, "Fixed field phase shifters for a multipass recirculating superconducting proton linac," *Phys. Rev. Accel. Beams*, vol. 24, no. 3, Mar. 2021, Art. no. 030101.